JGR Solid Earth

RESEARCH ARTICLE

Key Points:

- We extend 2D Epidemic Type Aftershock Sequence (ETAS) model to 3D to make use of high-precision hypocenter information
- Magnitude-dependent spatial power-law kernels with hypocentral distances best fit observed data
- Our 3D-ETAS model application reveals depth-dependent aftershock productivity in Southern California

Correspondence to:

B. M. Asayesh,
maleki@gfz-potsdam.de

Depth-Dependent Aftershock Trigger Potential Revealed by 3D-ETAS Modeling

Behnam M. Asayesh[1,2] , **Sebastian Hainzl[1,2]** , **and Gert Zöller[3]**

[1]GFZ German Research Centre for Geosciences, Potsdam, Germany, [2]Institute for Geosciences, University of Potsdam, Potsdam-Golm, Germany, [3]Institute of Mathematics, University of Potsdam, Potsdam-Golm, Germany

Abstract Current earthquake catalogs provide high-precision depth values that contain valuable information. Thus, we extend the spatiotemporal Epidemic Type Aftershock Sequence model to 3D by considering hypocentral instead of epicentral distances. To explore the most appropriate parametric form of the spatial kernel, we first examine different triggering functions for the depth difference of the aftershock-mainshock pairs identified by the Nearest-Neighbor method, showing that a magnitude-dependent power-law kernel fits best the earthquakes data in Southern California. Therefore, we incorporate the corresponding kernel into the 3D-ETAS model with space-dependent background activity, where we additionally allow for depth-dependent aftershock productivity. The application to Southern California shows that the model fits the data well. We also find that the aftershock productivity strongly depends on depth, similar to the seismic moment released by the mainshocks, which may be related to depth-dependent seismic coupling.

Plain Language Summary Seismicity models are an important backbone of seismic hazard analysis. So far, standard seismicity models are mostly restricted to epicenter information, neglecting earthquake depths because of historically large uncertainties. However, earthquake catalogs with high-precision depth values are nowadays available, enabling us to develop new statistical models, including hypocentral information. We first show that a power-law kernel best describes Southern California's hypocenter distribution of aftershocks. Thus, we incorporate it in our new seismicity model, which also considers a depth-varying background activity and aftershock potential. Our model consistently describes the observed earthquake occurrence and reveals a significant depth-dependent variation of the aftershock potential in Southern California.

1. Introduction

The Epidemic Type Aftershock Sequence (ETAS) model (Kagan & Knopoff, 1981, 1987; Ogata, 1988, 1998) is a widely used stochastic point process model for describing the distribution and clustering of earthquakes in space and time. According to the ETAS model, any earthquake, irrespective of its size, can trigger other (larger or smaller) earthquakes. This model fits the earthquake rate as a linear superposition of a constant background rate and decaying rates of ongoing aftershock sequences triggered by past events, where the expected number of triggered events (aftershock productivity) is an exponential function of magnitude, the temporal decay follows the Omori-Utsu law (Utsu, 1961), and the aftershocks spatial distribution is usually described by an isotropic power-law decay as a function of the epicentral distance to the source.

In the past decades, the ETAS model has been widely used and further developed in many applications (e.g., Console & Murru, 2001; Ebrahimian et al., 2022; Hainzl, 2021; Lombardi, 2015; Ogata et al., 2019; Werner et al., 2011; Zhuang, 2011; Zhuang et al., 2002, 2004, 2008). For historical reasons, this model is two-dimensional and uses only epicentral information because of the large depth uncertainties in the past. However, earthquake catalogs nowadays provide high-precision depth values that contain valuable information. Therefore, 3D versions of the ETAS model are desirable, exploiting the full hypocentral information of earthquake catalogs and providing the potential for modeling and forecasting seismicity with higher resolutions. Furthermore, the areas with complicated background tectonic, such as subduction zones consisting of inter- and intraplate seismicity, are too complex for 2D ETAS models, which ignores the depth of events (Ogata et al., 2019).

To utilize earthquake hypocenter data, Guo et al. (2015) extended the 2D-epicenter ETAS model to a 3D-hypocenter ETAS model. They assumed that the aftershock depth distribution is decoupled from the epicentral distribution and

follows a beta distribution for the relative position within the seismogenic zone. They applied the model first to Southern California (Guo et al., 2015) and second to the Kanto region (Guo et al., 2018). The results of this separable 3D model were validated through a comparison with results obtained from the 2D ETAS model. Recently Ogata et al. (2019) defined a flexible 3D hierarchical spatiotemporal ETAS model for seismicity forecasts beneath the greater Tokyo area.

Here, we develop a new 3D ETAS model that directly uses hypocentral distances in the spatial trigger function. To explore its most appropriate parametric form, we examine the empirical depth distribution of aftershocks as a function of the depth and magnitude of the mainshock. Unlike previous 3D ETAS studies (Guo et al., 2015, 2018) where depth effects have been separated from the horizontal 2D space, we consider a power-law spatial kernel with 3D-distance that accounts for the free surface and finite depth of the seismogenic zone by using horizontally and depth-dependent background rates. The model also allows to investigate a possible depth-dependence of the trigger potential. Aftershock productivity has been observed to vary widely for different mainshocks of similar size, which has been attributed to the plate boundary type (Boettcher & Jordan, 2004; Dascher-Cousineau et al., 2020), different source effects such as focal mechanisms and stress drops (Marsan & Helmstetter, 2017; Tahir & Grasso, 2015), and local effects such as seismic coupling and source depth (Dascher-Cousineau et al., 2020; Hainzl et al., 2019).

We apply the model to the Southern California catalog and estimate the 3D ETAS parameters and compare the resulting depth-dependent trigger potential with aftershocks selected by the Nearest-Neighbor (NN) approach.

2. ETAS Model Extension

In the ETAS model, the earthquake rate of $m \geq M_c$ events is defined by the sum of the background rate μ and the ongoing aftershock activity of all earthquakes that occurred before time t in or outside the target region. Its functional form is given by

$$R(\vec{x}, t) = \mu(\vec{x}) + \sum_{i:t_i < t} K \, 10^{\alpha(m_i - M_c)} (c + t - t_i)^{-p} f(|\vec{x} - \vec{x}_i|, m_i), \tag{1}$$

where $\vec{x}$ and $\vec{x}_i$ are 3D locations and earthquake hypocenters, that is, $\vec{x} = (x, y, z)$, instead of only horizontal distances and epicenters in the standard ETAS model. Here, all coordinates are in units of km. In particular, the spatial kernel is given by

$$\begin{aligned} f(|\vec{x} - \vec{x}_i|, m_i) &= c_n \left[d(m_i)^2 + r^2 \right]^{-(1+q)} \\ &= c_n(m_i) \left[(d_0 10^{\gamma m_i})^2 + (x - x_i)^2 + (y - y_i)^2 + (z - z_i)^2 \right]^{-(1+q)}. \end{aligned} \tag{2}$$

The normalization factor c_n is determined such that the integration over the 3D space is one. For a given radius R of the spherical integration, c_n is given by

$$c_n(m) = \left\{ \frac{4}{3} \pi R^3 d(m)^{-q-1} \, _2F_1\left(1.5, q+1, 2.5, -\left[\frac{R}{d(m)}\right]^2\right) \right\}^{-1} \tag{3}$$

with $_2F_1(\cdot, \cdot, \cdot, \cdot)$ being the Gauss hypergeometric function. Here, we use $R = 10^4$ km.

Note that using a separable spatial kernel like $c_n(m_i) f_{xy}\left(\sqrt{(x - x_i)^2 + (y - y_i)^2}\right) \cdot f_z(|z - z_i|)$, with power-law functions f_{xy} and f_z, is easier to handle from a numerical point of view. However, the functional form is unrealistic, as demonstrated in Figure S1 in Supporting Information S1.

For a given background rate, the ETAS parameters can be estimated by maximizing the log-likelihood ($\mathcal{LL}$) function for target earthquakes occurring in a given time-space volume $[T_1, T_2] \times [Z_1, Z_2] \times A$, where A is the surface area of the target region. $\mathcal{LL}$ is given by

$$\mathcal{LL} = \sum_{i=1}^{N} \ln\left[R(\vec{x}_i, t_i)\right] - \int_{T_1}^{T_2} \int_{Z_1}^{Z_2} \int_A R(x, y, z, t) \, dt \, dz \, d\vec{x}_{xy}, \tag{4}$$

where R includes the triggering effect of earthquakes occurring outside the target volume, for example, of events with $t < T_1$, $z < Z_1$, and $z > Z_2$.

2.1. Space-Dependent Background Rate

In reality, the background rate is variable, for example, due to different tectonic settings, and depth-dependent frictional strength and coupling. To estimate the background rate together with the other ETAS parameters, we extend the approach of Zhuang et al. (2002) to 3D. In this case, the background rate and ETAS parameters are iteratively and subsequently estimated until the solution of both converges. For the background rate estimation, adaptive smoothing of the observed events is applied using normal distributions, where the standard deviations are set to the distance to the M-nearest neighbor or a minimum value σ_{min}. In detail, the algorithm consists of the following steps:

1. Set M and σ_{min} and calculate, for each event (index i) in the target time-space volume, the epicentral distance to its Mth nearest epicenter ($r_{h,M,i}$) and, similarly, calculate the depth-distance to the Mth nearest event in depth ($r_{z,M,i}$).

2. Calculate the smoothing kernels for each event ($i = 1, \ldots, N$) used later for adaptive smoothing of the background rates. In x, y-direction, the smoothing is done by a two-dimension normal distribution $g_{2,i}$ with standard deviation $\sigma_{2,i} = \max\{r_{h,M,i}, \sigma_{min}\}$. In contrast, a renormalized one-dimensional normal distribution $g_{1,i}$ is used in z-direction with standard deviation $\sigma_{1,i} = \max\{r_{z,M,i}, \sigma_{min}\}$. $g_{1,i}$ is normalized such that the integral of $g_1(z - z_i, \sigma_{1,i})$ over the interval $[Z_1, Z_2]$ is one.

3. Set the probability p_b that an earthquake is a background event to 0.5 for all events, that is, $p_{b,i} = 0.5$ for $i = 1, \ldots, N$.

4. Calculate the background rate according to

$$\mu(\vec{x}) = \frac{\mu_f}{T_2 - T_1} \sum_{i=1}^{N} p_{b,i} \, g_1(z - z_i, \sigma_{1,i}) \, g_2\left(\sqrt{(x - x_i)^2 + (y - y_i)^2}, \sigma_{2,i}\right),$$ (5)

where factor μ_f is a free model parameter.

5. Estimate the parameters μ_f, K, α, c, p, d_0, γ, and q by maximizing the $\mathcal{LL}$-value in Equation 4 and store the corresponding $\mathcal{LL}_{max}$-value.

6. For all events, calculate the background probability $p_{b,i} = \mu(\vec{x}_i) / R(\vec{x}_i, t_i)$.

7. Repeat steps (4)–(6) until $\mathcal{LL}_{max}$ is converged. Here we require that the change of $\mathcal{LL}_{max}$ is less than 0.1.

Our standard choice was $M = 5$ and $\sigma_{min} = 0.5$ km, but we also tested the robustness of our result with other values (Supporting Information S1).

2.2. Depth-Dependent Trigger Potential

As a further extension, we consider that the trigger potential is depth-dependent. In particular, we assume that parameter K is a function of z according to

$$K(z) = K \cdot [1 + A \cdot h(z - Z_1, \tilde{\mu}, \tilde{\sigma}) \cdot H(z - Z_1)]$$ (6)

where H is the Heaviside function and h the lognormal distribution, $h(x, \tilde{\mu}, \tilde{\sigma}) = \exp\left(-\left[\ln(x) - \log(\tilde{\mu})\right]^2 / \left[2\tilde{\sigma}^2\right]\right) / \left(x\tilde{\sigma}\sqrt{2\pi}\right)$.

In this case, the number of model parameters N_p increases by three due to the additional parameters A, $\tilde{\mu}$, and $\tilde{\sigma}$. For comparison with the results of the ETAS model with uniform K-value, we use the Akaiki Information Criterion (AIC) given by $AIC = 2(N_p - \mathcal{LL}_{max})$, where the best model is given by the lowest AIC-value.

2.3. Numerical Simplifications

To speed up the computations, we use two approximations. First, we assume that the considered region A extends infinitely in horizontal directions for the second term in Equation 4. In this case, the integral I_i related to the spatial triggering kernel in the spatial integral

$$\int_V R(\vec{x}, t) \, d\vec{x} = \int_V \mu(\vec{x}) \, d\vec{x} + \sum_i K 10^{\alpha(m_i - M_c)} (c + t - t_i)^{-p} \, c_n(m_i) \, I_i$$

can be written in cylinder coordinates and after integrating with respect to the angle simplified to

$$I_i = \int_{Z_1}^{Z_2} \left\{ \int_0^\infty 2\pi r \left[(d_0 10^{\gamma m_i})^2 + r^2 + (z - z_i)^2 \right]^{-(1+q)} dr \right\} dz$$

$$= \frac{\pi}{q} \int_{Z_1}^{Z_2} \left[(d_0 10^{\gamma m_i})^2 + (z - z_i)^2 \right]^{-q} dz \qquad \text{for } q > 0$$

(7)

which allows facilitated, asymptotically unbiased estimation of ETAS parameters as in Schoenberg (2013).

Second, we limit the triggering of direct aftershocks to a maximum period of $T_{\max}$ after each event, while aftershock sequences can extend longer due to secondary triggering. Such a finite trigger time is expected from a physical point of view and may be statistically superior (Hainzl & Christophersen, 2017; Hainzl et al., 2016). A finite $T_{\max}$ speeds up the code's computation time, since the sum in Equation 1 is limited to the time period $[t - T_{\max}, t]$. Here we mainly use $T_{\max} = 1{,}000$ days but confirmed our results' robustness by testing larger values of 5,000 and 10,000 days (see Supporting Information S1).

Finally, we also ignore short-term aftershock incompleteness (STAI), which mainly affects small earthquakes shortly after a larger event (e.g., Hainzl, 2016; Kagan, 2004). While STAI can be directly considered in the $\mathcal{LL}$ approach (Hainzl, 2021), it increases the computational costs. Instead, we use an increased M_c value to reduce both computational costs and the effect of STAI.

3. Application

3.1. Data

The California data were downloaded from the Southern California Earthquake Data Center (SCEDC) and consist of 800,499 earthquakes recorded between 1 January 1981, and 31 March 2022 in the range of $-122°$ to $-113°$E and $30°–38°$N. According to Hutton et al. (2010), the catalog should be generally complete for $m \geq 2$ events. However, to minimize the effect of STAI after large events, we used $M_c = 3.0$ for the results presented in the main paper. The analyzed catalog consists of 15,534 $m \geq 3$ earthquakes, shown in Figure 1. For comparison, we also repeated our analysis for $M_c = 2.0$, including 143,353 catalog events, with corresponding results shown in Supporting Information S1.

3.2. Nearest-Neighbor Event Association

To compare the ETAS model, we alternatively define the background events and aftershocks by the NN method (Baiesi & Paczuski, 2004, 2005; Zaliapin et al., 2008). The method quantifies the correlation between an event i and a preceding event j by its magnitude-weighted space-time distance $n_{ij} = (t_i - t_j) |\vec{x}_i - \vec{x}_j|^d 10^{-bm_j}$ with t, $\vec{x}$, and m being the time, hypocenter, and magnitude of the events, respectively. The Gutenberg-Richter b-value is set to 1.0. The fractal dimension d of the hypocenter distribution, which would be $d = 2$ for a uniform planar distribution and $d = 3$ for a uniform distribution in 3D, is set to $d = 2.3$. This distance can be written as $n_{ij} = T_{ij} R_{ij}$ with rescaled time $T_{ij} = (t_i - t_j)10^{-0.5bM_j}$ and rescaled distance $R_{ij} = |\vec{x}_i - \vec{x}_j|^d 10^{-0.5bM_j}$. Among all events j preceding i, the (most likely) trigger of i is the event with the lowest n_{ij}-value. A threshold value of n_c is set to distinguish between triggered and background activity, and only events with $n_{ij} \leq n_c$ are considered plausible parent-aftershock pairs. Here, the parent event is the most likely event which triggered the aftershock but not necessarily the largest event within the corresponding aftershock sequence.

Figure S2 in Supporting Information S1 provides the $\log_{10}(R)$ versus $\log_{10}(T)$ distribution showing that $n_c = -4.5$ is a good discriminator if time is measured in units of year and distances in km units.

3.3. Stacked Relative Depth Triggering

In order to test different kernels for depth difference of the parent-triggered pairs identified by the NN approach, we use Normal, Exponential, and Power-law distributions (Table 1 and Figure 2 for best fits). We also test a magnitude-dependence of the distributions by considering $d = d_0 10^{\gamma M_m}$ and estimate parameters by maximizing the log-likelihood function. The power-law distribution shows the best performance according to AIC (see Table 1). Similar results are obtained for the events with $m \geq 2$, as shown in Figure S3 and Table S1 in Supporting Information S1.
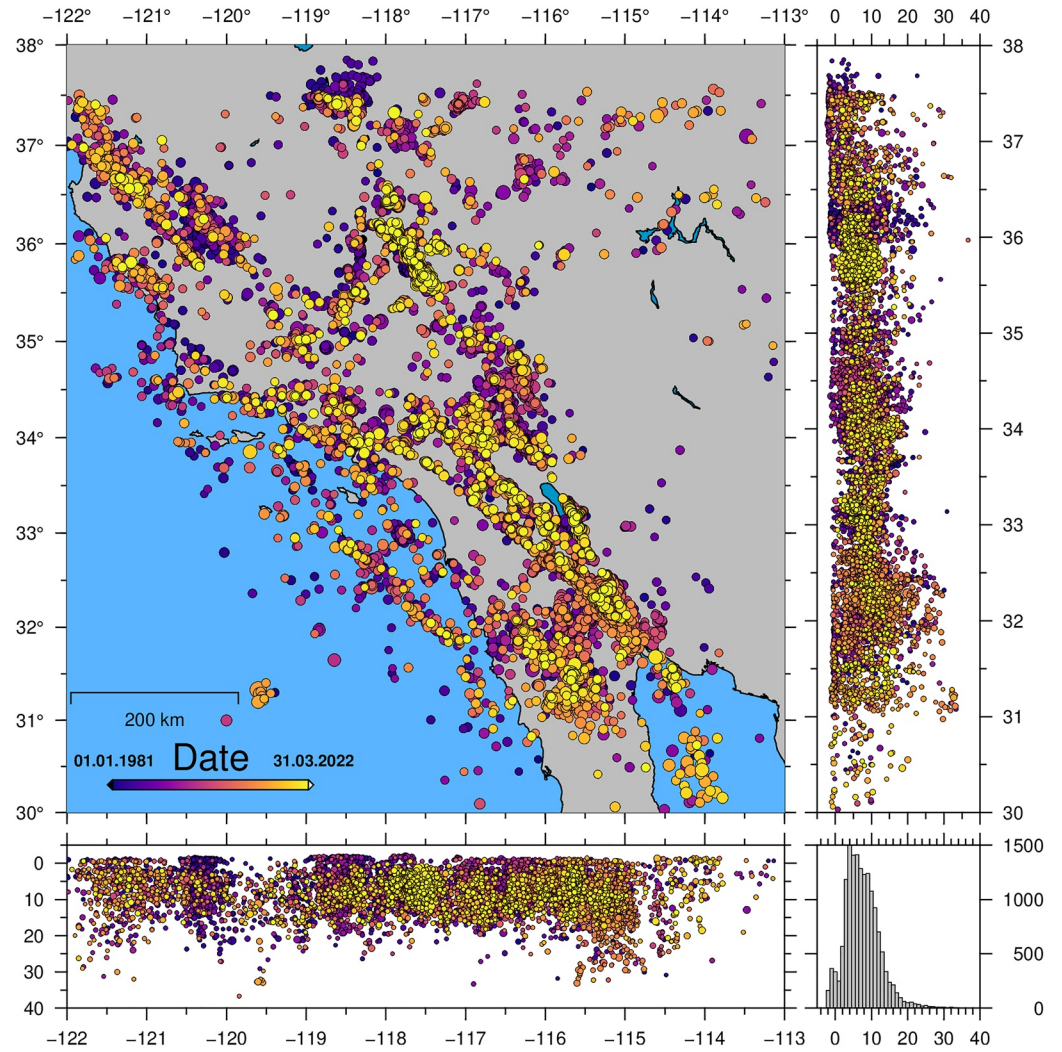
Figure 1. Map view of the epicenter and depth distribution of $m \geq 3$ seismicity between 1 January 1981, and 31 March 2022 in southern California from relocated catalog (Hauksson et al., 2012). The color of the circles represents time and the histogram at the bottom right shows the depth distribution of the events.

Table 1
Test of Different Spatial Kernels as a Function of the Difference in the Event Depths

Kernel	Probability density	d	d_0	γ	q	ΔAIC[a]
Normal	$\sim\exp\left(-\Delta z^2/\left(2d^2\right)\right)$	4.27	–	–	–	0
Normal(m)	$\sim\exp\left(-\Delta z^2/\left(2d(m)^2\right)\right)$	–	0.39	0.18	–	4,643
Exponential	$\sim\exp\left(-|\Delta z|/d\right)$	2.15	–	–	–	3,612
Exponential(m)	$\sim\exp\left(-|\Delta z|/d(m)\right)$	–	0.07	0.28	–	11,859
Power-law	$\sim(d+|\Delta z|)^{-(1+q)}$	0.05	–	–	1.05	11,580
Power-law(m)	$\sim(d(m)+|\Delta z|)^{-(1+q)}$	–	0.003	0.52	2.09	17,495

Note. The parameters stem from the maximum likelihood estimation of the parent-aftershock pairs identified by the NN approach.

[a]$\Delta AIC = AIC_{\text{Normal}} - AIC$, where the largest value indicates the best model.
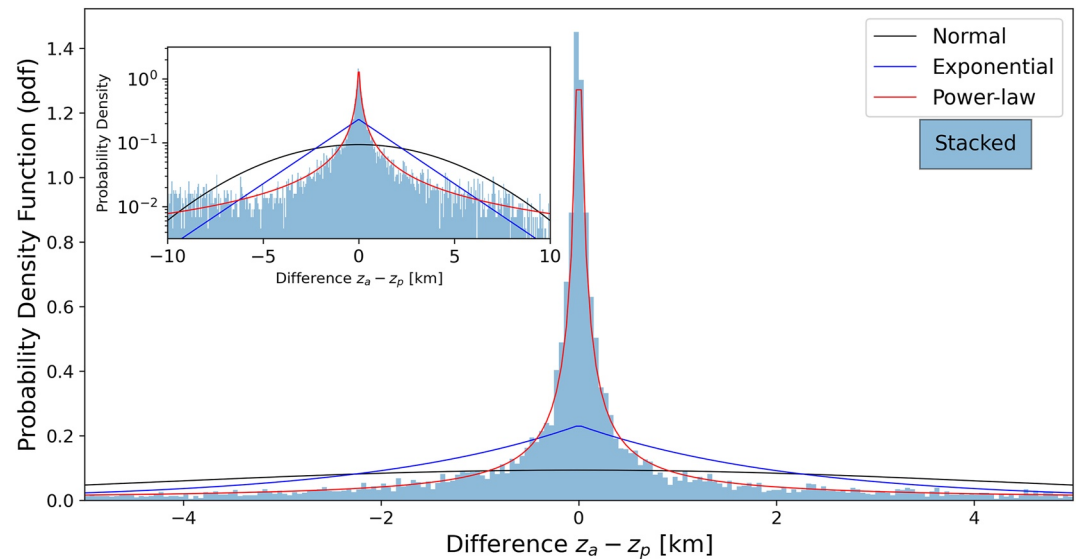
Figure 2. Probability density function (pdf) of the difference between the hypocentral depths of the aftershocks (z_a) and parents (z_p) selected by the Nearest-Neighbor method (filled area). The curves refer to the fits of the Normal distribution (black line), Exponential distribution (blue line), and Power-law distribution (red line). The inset plot shows the same results on a log-linear scale.

Note that this analysis considers so far only the distance in depth while ignoring the epicentral distances of the event pairs. In particular, the stacked activity in Figure 2 consists of events with very different epicentral distances. In contrast, hypocentral distances are directly considered in the following 3D-ETAS application.

3.4. ETAS Fits

We estimate the ETAS parameters together with a 3D varying background rate. For this purpose, we assume a constant K-value in the first step. Then, we consider a depth-dependent trigger potential in a second step by assuming that K varies with depth according to Equation 6.

Table 2 provides the results using events that occurred after the starting time T_s = 1/1/1991 by considering smoothing kernels with standard deviations related to the M = 5th nearest neighbors and a minimum value of σ_{min} = 0.5 km for the background rate estimation. The depth interval of the fit was set to Z_1 = 0 and Z_2 = 30 km and the maximum duration for triggering direct aftershocks was set to T_a = 1,000 days. However, we verified the robustness of our result with other values for the hyperparameters T_s, T_a, M, and σ_{min} (Tables S2–S5 in Supporting Information S1).

We can use the AIC values to compare the results for different hyperparameters and those of the 3D ETAS models with depth-dependent and uniform K-values. The results (Table 2 and Tables S2–S5 in Supporting Information S1) confirm that the 3D ETAS model with depth-dependent K-value fits significantly better to the Southern California data than the model with constant K. Furthermore, the fits improve for small M and σ_{min} values (Tables

Table 2
Estimated 3D Epidemic Type Aftershock Sequence (ETAS) and 2D ETAS Parameters for Events After T_s = 1/1/1991, Using Parameters T_a = 1,000 Days, M = 5, and σ_{min} = 0.5 km

Model	μ[a] (1/d)	K	α	c (d)	p	d_0	γ	q	A	$\tilde{\mu}$	$\tilde{\sigma}$	AIC
ETAS[b]	0.35	0.0284	0.52	0.005	1.12	0.008	0.41	0.82	–	–	–	203,965
ETAS[c]	0.35	0.0039	0.59	0.005	1.12	0.007	0.42	0.76	103.3	8.5	0.79	203,085
ETAS[d]	0.32	0.0251	0.55	0.004	1.09	0.019	0.34	0.46	–	–	–	–

[a]Total background rate in the target volume. [b]ETAS model with uniform K-value. [c]ETAS model with depth-dependent K-value according to Equation 6. [d]2D ETAS model.
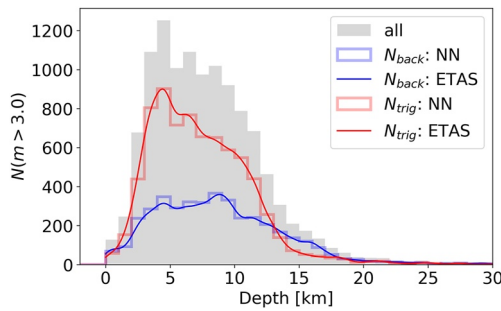
Figure 3. Depth distribution of all $m \geq 3$ earthquakes (gray) and those identified by the Nearest-Neighbor (NN) method as aftershocks (red steps) and background events (blue steps). The colored smooth curves refer to the corresponding results of the 3D Epidemic Type Aftershock Sequence (ETAS) model. The corresponding lateral variation of the estimated background rates is shown in the Figure S4 in Supporting Information S1 for four different depth layers.

S4 and S5 in Supporting Information S1). Further minor improvement is achieved for increasing T_a (Table S3 in Supporting Information S1).

There is no significant difference in the parameters of the spatial kernel (γ, d_0, and q) for different tested values. The γ and d_0 values are similar for the fits with uniform K-value and depth-dependent K-value; just γ increases by a hundredth and d_0 decreases by a thousandth for the second approach. Furthermore, γ is similar to the estimated value in Table 1 for the power-law spatial kernel applied to depth differences. On the other hand, q shows a slight decrease for the ETAS model with depth-dependent K-value. The parameters p and c of the Omori-Utsu law and total background seismic rate in the time-space target volume (μ) are the same for both model versions, but they slightly change for different hyperparameters. The α value slightly increases for the ETAS model with a depth-dependent K-value (Table 2 and Tables S2–S5 in Supporting Information S1).

From a physical point of view, $d(m) = d_0 10^{\gamma m}$ of the spatial triggering kernel can be expected to scale with the rupture dimension (R_d) of the earthquake. For small earthquakes with R_d significantly less than the seismogenic width, circular ruptures are expected with R_d being related to the rupture area (A) according to $R_d = \sqrt{A/\pi}$. Empirical relations show a magnitude scaling of $A = 10^{c_1+c_2 m}$ with c_2 close to 1.0. In particular, Wells and Coppersmith (1994) found $c_2 = 0.91$ (0.90) for all (strike-slip) rupture mechanisms, corresponding to $R_d(m) \sim 10^{0.5 c_2 m} = 10^{\tilde{\gamma} m}$ with $\tilde{\gamma} = 0.46$ (0.45). The empirical scaling coefficient $\tilde{\gamma}$ of the rupture dimension is thus a little bit larger than the revealed scaling coefficient of the aftershock triggering, $\gamma = 0.42$ (Table 2). However, larger earthquakes experience the limits of the seismogenic zone, leading to a smaller scaling coefficient of the down-dip rupture width, namely 0.32 (0.27) for all (strike-slip) earthquakes according to Wells and Coppersmith (1994), respectively 0.41 (0.33) according to Blaser et al. (2010). Thus, our derived value lies in the range of the rupture scaling parameters.

3.5. Comparison With 2D ETAS

To compare the parameters estimated by our new 3D ETAS model with those of the traditional 2D ETAS model, we used the same model framework and data, only replacing the hypocenter with the epicenter locations and omitting the term $(z - z_i)^2$ in Equation 2 and $g_1(z - z_i, \sigma_{1,i})$ in Equation 5. The resulting parameters, shown in the third row of Table 2, are found to be very similar to those of the ETAS 3D, with almost identical temporal decay parameters and only minor differences in the productivity scaling with magnitude. However, there are some differences in the shape of the spatial trigger function, namely a smaller $\gamma = 0.34$ and $q = 0.46$ values compared to the best 3D ETAS model ($\gamma = 0.42$ and $q = 0.76$). Note that we cannot compare the AIC value of the 2D ETAS model with that of the 3D ETAS model because R in Equation 4 is a 2D-density rate in the former case and a 3D-density rate in the latter case (different units).

3.6. Comparison With NN-Distributions

To verify the results of our new 3D ETAS model, we compare the cluster selection and declustering results of our 3D ETAS by comparing them with the results of the independent, well-established NN method for cluster selection and declustering in 3D. For this purpose, we first estimate the background probability (p_b) of all events by the ratio between the background rate and the total earthquake rate at the events' occurrence time and location (see Section 2.1, step 6). Conversely, the probability of being an aftershock is given by $1 - p_b$. Then, the number of background and triggered events are estimated for different depth bins by summing the probability values. Figure 3 shows the resulting distributions (smooth curves) for the $m \geq 3$ earthquakes in Southern California (from 1 January 1991 to 31 March 2022) in comparison to those identified for the same data by the NN method (steps). The corresponding comparison of joint distributions of the rescaled time T and space R values are presented in Figure S5 in Supporting Information S1. The results for the 3D ETAS model and NN approach are similar, verifying the consistency of our new 3D ETAS model.

In the next step, we compare the probability density distribution of the difference between the hypocentral depths of the aftershocks and parent events in different depth ranges of the parent events. Results for six different depth
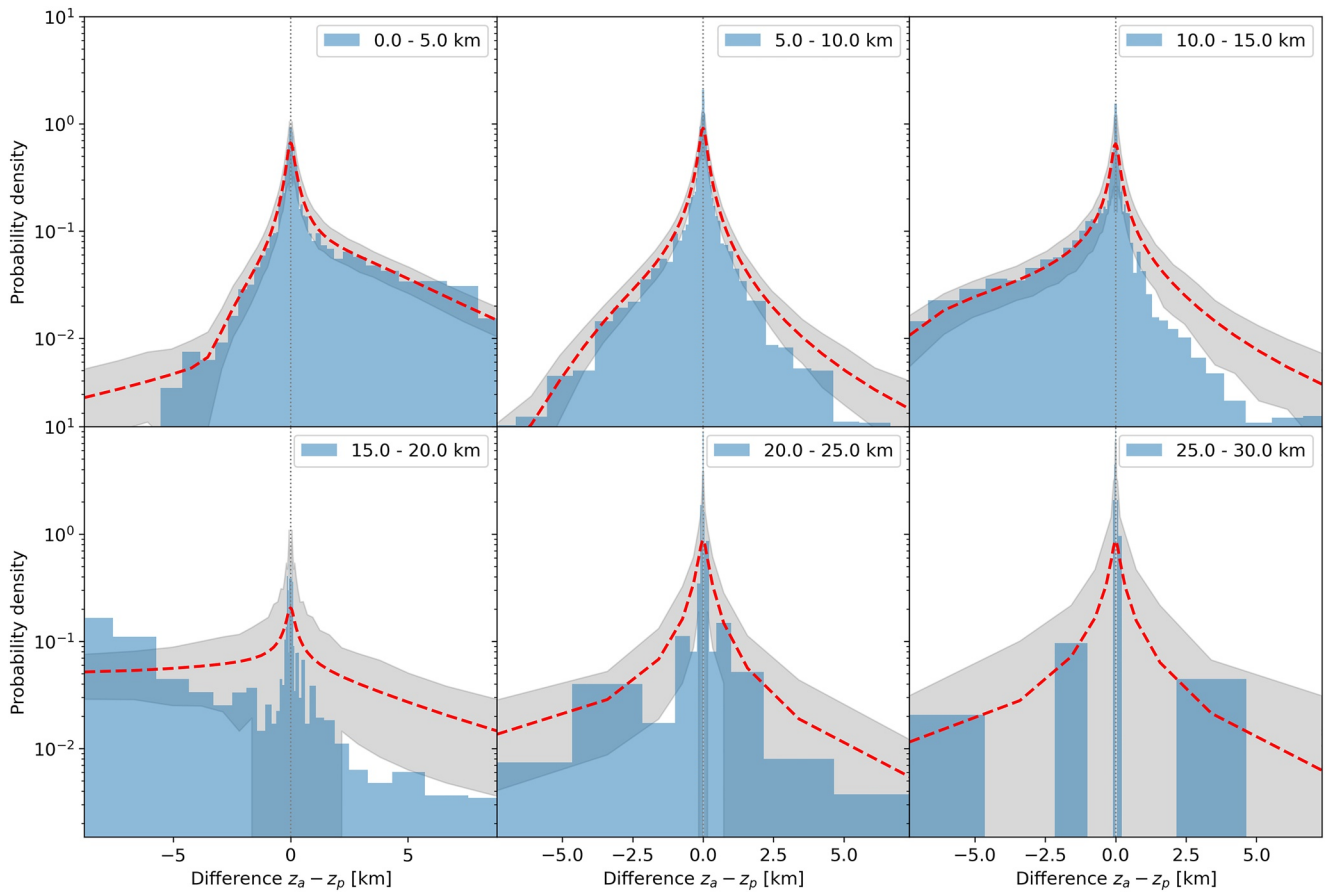
Figure 4. Probability density distribution of the difference between the hypocentral depths of the aftershocks (z_a) and parent events (z_p) as a function of the depth of the parent event. The selected depth ranges of the parent events are provided in the legend of each panel. The filled distribution refers to the stacked pairs of ($M_c = 3.0$) selected by the Nearest-Neighbor method. For the same parent events, the dashed red curve shows the correspondent theoretical forecast of the Epidemic Type Aftershock Sequence model using the parameters estimated by the maximum likelihood method for $M_c = 3.0$, where the gray shaded area refers to the 90% confidence interval. For better visualization, exponentially increasing bin sizes are used with distance.

ranges for the parents are depicted in Figure 4. The parent events in each depth range are selected by the NN approach using the $m \geq 3$ events in the target period (from 1 January 1991 to 31 March 2022). In each panel, the probability density distribution of the corresponding NN-identified aftershocks is shown as filled distribution. We calculated the theoretical forecast of the 3D ETAS model related to the same parent events by using the parameters estimated by the maximum likelihood method for the model with depth-dependent K-value (Table 2). The dashed red curves show the ETAS predictions, where the gray shaded areas refer to the 90% confidence intervals. A similar analysis for $M_c = 2.0$ is presented in Figure S6 in Supporting Information S1. Overall, the ETAS-based predictions agree with the empirical NN results for most of the depth ranges of the parent events, independent of whether the parent event occurs close to the surface or at a larger depth. The only significant deviation is observed in depth ranges 10–15 and 15–20 km, where the ETAS model slightly overestimates the down-dip aftershocks.

Finally, we also confirmed the consistency of the assumed spatial power-law kernel by stochastic reconstruction of the triggering kernel (see Zhuang et al., 2004). Details and the results are provided in Supporting Information S1. Figure S7 in Supporting Information S1 shows that the theoretical kernel agrees well with the reconstructed values, in particular the model with depth-dependent K shows the best fit.

3.7. Depth-Dependent Productivity

Figure 3 indicates different shapes of the background and aftershock distributions. While the background activity has a broad peak within 4–10 km depth, the aftershock activity peaks more sharply around 5 km. To explore
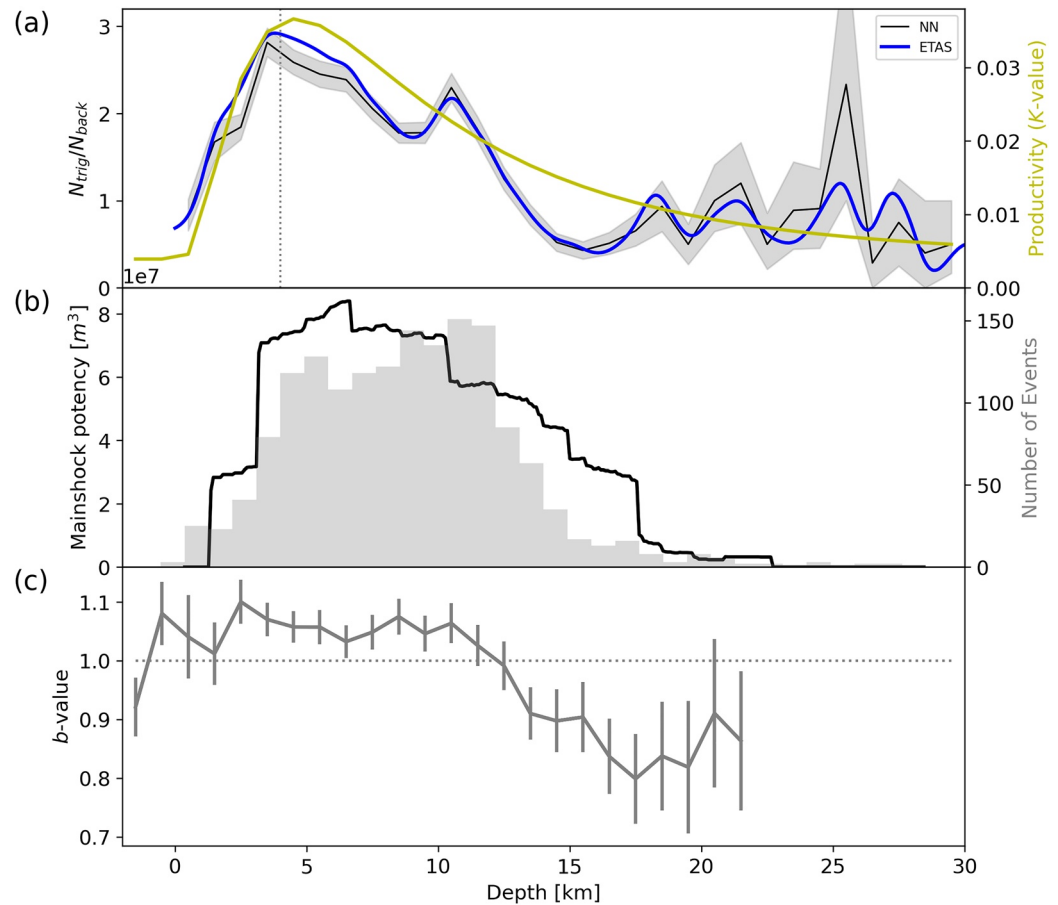
Figure 5. Depth-dependence of the earthquake properties in California: (a) The ratio between triggered and background events, identified by Nearest-Neighbor (NN) (black) and Epidemic Type Aftershock Sequence (ETAS) (blue), with the scale on the left. The gray shaded area corresponds to the 90% confidence interval assuming a Poisson distribution. The yellow curve (with the scale on the right) refers to the estimated variation of the K-value with depth. The dotted vertical gray line indicates the depth of 4 km where the ratio of triggered to background events and the K value approximately peak. (b) Cumulative seismic potency released co-seismically by mainshocks in the study region (black curve, left scale) and the aftershock distribution of these mainshocks (gray bars, right scale). (c) Variations of the b-value with error bars referring to plus/minus one standard deviation. The dotted horizontal line refers to $b = 1$.

the difference, we calculated the normalized aftershock number, that is, the ratio between the aftershock and background events, as a function of depth. The results are shown in Figure 5a for NN (black curve) and ETAS (blue curve). The derived ratio is below one close to the surface, peaks around 4 km depth with a value of approximately three (dotted vertical gray line in Figure 5a), and decays again to values below one at a depth of approximately 13 km. The changing ratio does not necessarily refer to differences in the ETAS aftershock productivity parameters. The NN-derived ratio of triggered events to background events can be biased by the fact that larger earthquakes may preferentially occur at certain depths, for example, due to a smaller b or a larger M_{max}. Since larger events tend to trigger more aftershocks than smaller events, this would increase the ratio of triggered to background events at that depth. This would also happen if the aftershock productivity (K value) is constant at depth, but in this case the ETAS model would reveal a constant K because it takes into account the actual earthquake magnitudes. However, the ETAS-derived depth-dependence of the K value (yellow curve with the scale on the right) has a very similar shape, confirming that the changes in the ratio are related to varying aftershock productivity with depth.

For comparison, we show in Figure 5 the depth-dependence of the aftershock productivity together with other earthquake properties. First, we use finite-fault rupture models from the SRCMOD (http://equake-rc.info/srcmod/) database by Mai and Thingbaijam (2014) to analyze the seismic potency release in different depths which may approximate the cumulative brittle slip and thus be linearly correlated with seismic coupling. Our

analysis consists of 38 slip models from 16 mainshocks in the study area since 1979 (Table S6 in Supporting Information S1). For this purpose, we discretized the depth in bins of 0.1 km and calculated, for each mainshock, the released seismic potency, that is, the product of rupture area times slip, in the bins. If several alternative slip models exist, we determined the average potency release for the mainshock and finally summed the results for all mainshocks. The result is shown in Figure 5b. We find a high correlation between seismic potency released by the mainshocks and the revealed aftershock productivity. The corresponding Pearson correlation coefficient is 0.72 with a probability (*p*-value) to be uncorrelated of less than 1e-5. In the same panel (scale on the right), we also show the distribution of the direct aftershocks triggered by these 16 mainshocks according to the NN method.

We also explore the depth-dependence of the *b*-value for our data set ($m \geq 3$). Here, we use the maximum likelihood method for the *b*-value estimation (Aki, 1965), with results shown in Figure 5c. For shallow depth (<12 km), the *b*-value is larger than 1.0 with a moderate decreasing trend with increasing depth. However, below approximately 12 km, it decreases more quickly, similar to the mainshock potency and the aftershock productivity. The Pearson's correlation coefficient is 0.82 with *p*-value < 3e-6 between the depth-dependence of the *b*-value and that of the aftershock productivity in the 0–22 km depth range. The corresponding correlation coefficients of the *b*-value with the background rate and the mainshock potency are both 0.81 with *p*-values less than 4e-6.

4. Discussion

Our 3D ETAS model considers depth-dependent background rates and trigger potential. Both are found to vary significantly with depth (Figures 3 and 5a), with peaks at intermediate depths. Both distributions correlate well with other earthquake properties. In particular, we revealed a high correlation between the aftershock productivity and the released seismic potency of the mainshocks in California.

Previous studies have already linked different aftershock productivity to different site conditions or mainshock source effects. According to Tahir and Grasso (2015), the aftershock productivity depends on the focal mechanism of the mainshock. By analyzing global earthquake catalogs, they found that thrust events have larger *K*-values and background rates compared to strike-slip mainshocks. However, there is significant regional variation in aftershock productivity (Page et al., 2016). Recently, Dascher-Cousineau et al. (2020) synthesized multiple possible relationships between aftershock productivity and earthquake location effects such as plate boundary type, depth, and lithospheric age; and source effects such as radiated energy, stress drop, source geometry, and slip heterogeneity. Their analysis for global catalog data showed that the source effects stress drop, normalized rupture width, and rupture's aspect ratio and the location properties of the lithosphere age, plate boundary, and the earthquake depth correlate well with earthquake productivity. In particular, the aftershock productivity was found to decrease with depth, which is in general agreement with our results.

We hypothesize that the observed depth dependence of the aftershock productivity in California relates to seismic coupling. For a case study in northern Chile, Hainzl et al. (2019) showed that the aftershock productivity is linearly related to the geodetically derived coupling of the subduction interface. While such a detailed analysis is not feasible for the distributed fault system in Southern California, it is reasonable to assume that similar mechanisms apply. The same (earthquake-induced) stress changes can initiate more aftershocks in areas with a high density of asperities (velocity-weakening areas), that is, in areas with high coupling, compared to areas dominated by creep and few asperities, that is, low coupling.

This interpretation is generally consistent with the explanation of Dascher-Cousineau et al. (2020) that changes in the aftershock productivity are due to variations in the ability of the mainshock to brittly deform the surrounding volume. Furthermore, our hypothesis is also consistent with the observation that aftershock productivity negatively correlates with heat flow, interpreted in the context of a temperature-dependent rheology (Yang & Ben-Zion, 2009), since high heat flow is expected to reduce the fault coupling.

The observed shape of the aftershock productivity, like that of the background rate (Figure 3), resembles, to some degree, the estimated *b*-value dependence. Evidence from different studies ranging from laboratory scale to observations for induced and natural seismicity in different tectonic regimes suggests that the *b*-value is negatively correlated with differential stress (e.g., Amitrano, 2003; Öncel & Wyss, 2000; Scholz, 1968; Tormann et al., 2012). In our case, the *b*-value decreases monotonically with depth in the range of ~4–17 km, with the most significant changes below 10 km (Figure 5c). This observation is in agreement with the results of Spada

et al. (2013), who studied California and six other continental areas around the world. The simultaneous decrease in aftershock productivity and b-value with depth indicates that earthquakes in deeper zones are less likely to be triggered, which may be due to lower coupling at deeper depths. However, they become, on average, larger if they nucleate.

Note that the aftershock productivity in California is also likely to vary laterally, as indicated by varying clustering characteristics (Zaliapin & Ben-Zion, 2013). It would be desirable to account for this in our model, but this would require a non-parametric estimation with a significantly increased number of free parameters. It was therefore beyond the scope of this study.

The developed new 3D ETAS model uses an isotropic spatial kernel. However, the spatial distribution of aftershocks around the mainshock is generally not isotropic. Many studies show that anisotropic spatial distribution of aftershocks correlates well with coseismic stress changes due to mainshock (e.g., Asayesh, Zafarani, et al., 2020; Asayesh, Zarei, et al., 2020; Hainzl et al., 2010; King et al., 1994; Meade et al., 2017; Sharma et al., 2020). The assumption of isotropic aftershock distributions in the ETAS model can significantly bias the estimation of the model parameters, in particular, the α value (Hainzl et al., 2008). Taking the anisotropy into account can significantly improve forecasts (Bach & Hainzl, 2012; Grimm et al., 2022). Thus, it would be desirable to include the stress effects of mainshocks in the 3D ETAS model as recently suggested by Asayesh et al. (2022), who suggested the implementation of simple stress metrics in the spatiotemporal ETAS model. Consequently, a natural extension of our current work will be implementing such 3D stress-based kernels for large earthquakes with additional source information in the 3D ETAS model to consider anisotropic aftershock distributions.

5. Conclusions

The developed 3D ETAS model can exploit precise hypocentral information nowadays available in current catalogs. Our model extension can help improve detailed seismicity modeling and avoid biased parameter estimation resulting from the use of epicentral rather than hypocentral distances between earthquakes. In order to incorporate the earthquakes' depth information in the ETAS model, we simply extended the established 2D spatial power-law kernel by using hypocentral instead of epicentral distances. The comparison with independent NN results and stochastic reconstruction shows that this triggering kernel fits well with the earthquake pattern in Southern California. The developed model can also handle spatially varying background activity in all directions and account for a depth-dependent trigger potential.

The application to the Southern California earthquake catalog reveals a depth-dependent background rate and a significantly variable aftershock trigger potential with depth. The latter peaks at a depth of approximately 5 km with a triggering potential increased by a factor of more than three compared to shallower and deeper regions. A similar variation is also observed for the cumulative seismic potency released co-seismically by the mainshocks in the same region. Previous observations in Northern Chile (Hainzl et al., 2019) revealed a linear relationship between the aftershock trigger potential and seismic coupling, which could also explain our observations for Southern California.

In conclusion, the developed 3D ETAS model can provide new information on the depth-dependent properties of seismicity, more detailed 3D modeling of earthquake sequences, and may help to improve forecasting. Finally, it can be simply extended to replace the isotropic triggering kernel with physical stress-based triggering kernels for large earthquakes for which additional source information is available.

Data Availability Statement

The Southern California earthquake catalog has been downloaded from the Southern California Earthquake Data Center (SCEDC, https://scedc.caltech.edu/data/alt-2011-dd-hauksson-yang-shearer.html, last accessed December 2022) and all the slip data are freely available on http://equake-rc.info/srcmod/.

References

Aki, K. (1965). Maximum likelihood estimate of *b* in the formula logN=*a-b*M and its confidence limits. *Bulletin of the Earthquake Research Institute, University of Tokyo*, *43*, 237–239.

Amitrano, D. (2003). Brittle-ductile transition and associated seismicity: Experimental and numerical studies and relationship with the *b* value. *Journal of Geophysical Research*, *108*(B1), 2044. https://doi.org/10.1029/2001jb000680

Asayesh, B. M., Zafarani, H., Hainzl, S., & Sharma, S. (2022). Effects of large aftershocks on spatial aftershock forecasts during the 2017–2019 western Iran sequence. *Geophysical Journal International*, *232*(1), 147–161. https://doi.org/10.1093/gji/ggac333

Asayesh, B. M., Zafarani, H., & Tatar, M. (2020). Coulomb stress changes and secondary stress triggering during the 2003 (Mw 6.6) Bam (Iran) earthquake. *Tectonophysics*, *775*, 228304. https://doi.org/10.1016/j.tecto.2019.228304

Asayesh, B. M., Zarei, S., & Zafarani, H. (2020). Effects of imparted Coulomb stress changes in the seismicity and cluster of the December 2017 Hojedk (SE Iran) triplet. *International Journal of Earth Sciences*, *109*(7), 2307–2323. https://doi.org/10.1007/s00531-020-01901-0

Bach, C., & Hainzl, S. (2012). Improving empirical aftershock modeling based on additional source information. *Journal of Geophysical Research*, *117*(B4), B04312. https://doi.org/10.1029/2011jb008901

Baiesi, M., & Paczuski, M. (2004). Scale-free networks of earthquakes and aftershocks. *Physical Review E*, *69*(6), 066106. https://doi.org/10.1103/physreve.69.066106

Baiesi, M., & Paczuski, M. (2005). Complex networks of earthquakes and aftershocks. *Nonlinear Processes in Geophysics*, *12*, 1–11. https://doi.org/10.5194/npg-12-1-2005

Blaser, L., Krüger, F., Ohrnberger, M., & Scherbaum, F. (2010). Scaling relations of earthquake source parameter estimates with special focus on subduction environment. *Journal of Geophysical Research*, *100*(6), 2914–2926. https://doi.org/10.1785/0120100111

Boettcher, M., & Jordan, T. (2004). Earthquake scaling relations for mid-ocean ridge transform faults. *Journal of Geophysical Research*, *109*(B12), B12302. https://doi.org/10.1029/2004jb003110

Console, R., & Murru, M. (2001). A simple and testable model for earthquake clustering. *Journal of Geophysical Research*, *106*(B5), 8699–8711. https://doi.org/10.1029/2000jb900269

Dascher-Cousineau, K., Brodsky, E. E., Lay, T., & Goebel, T. H. (2020). What controls variations in aftershock productivity? *Journal of Geophysical Research: Solid Earth*, *125*(2), e2019JB018111. https://doi.org/10.1029/2019jb018111

Ebrahimian, H., Jalayer, F., Maleki Asayesh, B., Hainzl, S., & Zafarani, H. (2022). Improvements to seismicity forecasting based on a Bayesian spatio-temporal ETAS model. *Scientific Reports*, *12*(1), 1–27. https://doi.org/10.1038/s41598-022-24080-1

Grimm, C., Hainzl, S., Käser, M., & Küchenhoff, H. (2022). Solving three major biases of the ETAS model to improve forecasts of the 2019 Ridgecrest sequence. *Stochastic Environmental Research and Risk Assessment*, *36*(8), 2133–2152. https://doi.org/10.1007/s00477-022-02221-2

Guo, Y., Zhuang, J., & Hirata, N. (2018). Modelling and forecasting three-dimensional-hypocentre seismicity in the Kanto region. *Geophysical Journal International*, *214*(1), 520–530. https://doi.org/10.1093/gji/ggy154

Guo, Y., Zhuang, J., & Zhou, S. (2015). A hypocentral version of the space-time ETAS model. *Geophysical Journal International*, *203*(1), 366–372. https://doi.org/10.1093/gji/ggv319

Hainzl, S. (2016). Rate-dependent incompleteness of earthquake catalogs. *Seismological Research Letters*, *87*(2A), 337–344. https://doi.org/10.1785/0220150211

Hainzl, S. (2021). ETAS-approach accounting for short-term incompleteness of earthquake catalogs. *Bulletin of the Seismological Society of America*, *112*(1), 494–507. https://doi.org/10.1785/0120210146

Hainzl, S., Brietzke, G. B., & Zöller, G. (2010). Quantitative earthquake forecasts resulting from static stress triggering. *Journal of Geophysical Research*, *115*(B11), B11311. https://doi.org/10.1029/2010jb007473

Hainzl, S., & Christophersen, A. (2017). Testing alternative temporal aftershock decay functions in an ETAS framework. *Geophysical Journal International*, *210*(2), 585–593. https://doi.org/10.1093/gji/ggx184

Hainzl, S., Christophersen, A., & Enescu, B. (2008). Impact of earthquake rupture extensions on parameter estimations of point-process models. *Bulletin of the Seismological Society of America*, *98*(4), 2066–2072. https://doi.org/10.1785/0120070256

Hainzl, S., Christophersen, A., Rhoades, D., & Harte, D. (2016). Statistical estimation of the duration of aftershock sequences. *Geophysical Journal International*, *205*(2), 1180–1189. https://doi.org/10.1093/gji/ggw075

Hainzl, S., Sippl, C., & Schurr, B. (2019). Linear relationship between aftershock productivity and seismic coupling in the Northern Chile subduction zone. *Journal of Geophysical Research: Solid Earth*, *124*(8), 8726–8738. https://doi.org/10.1029/2019jb017764

Hauksson, E., Yang, W., & Shearer, P. (2012). Waveform relocated earthquake catalog for southern California (1981 to 2011). *Bulletin of the Seismological Society of America*, *102*(5), 2239–2244. https://doi.org/10.1785/0120120010

Hutton, K., Woessner, J., & Hauksson, E. (2010). Earthquake monitoring in southern California for seventy-seven years (1932–2008). *Bulletin of the Seismological Society of America*, *100*(2), 423–446. https://doi.org/10.1785/0120090130

Kagan, Y. Y. (2004). Short-term properties of earthquake catalogs and models of earthquake source. *Bulletin of the Seismological Society of America*, *94*(4), 1207–1228. https://doi.org/10.1785/012003098

Kagan, Y. Y., & Knopoff, L. (1981). Stochastic synthesis of earthquake catalogs. *Journal of Geophysical Research*, *86*(B4), 2853–2862. https://doi.org/10.1029/jb086ib04p02853

Kagan, Y. Y., & Knopoff, L. (1987). Statistical short-term earthquake prediction. *Science*, *236*(4808), 1563–1567. https://doi.org/10.1126/science.236.4808.1563

King, G. C., Stein, R. S., & Lin, J. (1994). Static stress changes and the triggering of earthquakes. *Bulletin of the Seismological Society of America*, *84*(3), 935–953.

Lombardi, A. M. (2015). Estimation of the parameters of etas models by simulated annealing. *Scientific Reports*, *5*(1), 1–11. https://doi.org/10.1038/srep08417

Mai, P. M., & Thingbaijam, K. (2014). SRCMOD: An online database of finite-fault rupture models. *Seismological Research Letters*, *85*(6), 1348–1357. https://doi.org/10.1785/0220140077

Marsan, D., & Helmstetter, A. (2017). How variable is the number of triggered aftershocks? *Journal of Geophysical Research: Solid Earth*, *122*(7), 5544–5560. https://doi.org/10.1002/2016jb013807

Meade, B. J., DeVries, P. M., Faller, J., Viegas, F., & Wattenberg, M. (2017). What is better than Coulomb failure stress? A ranking of scalar static stress triggering mechanisms from 105 mainshock-aftershock pairs. *Geophysical Research Letters*, *44*(22), 11–409. https://doi.org/10.1002/2017gl075875

Ogata, Y. (1988). Statistical models for earthquake occurrences and residual analysis for point processes. *Journal of the American Statistical Association*, *83*(401), 9–27. https://doi.org/10.1080/01621459.1988.10478560

Ogata, Y. (1998). Space-time point-process models for earthquake occurrences. *Annals of the Institute of Statistical Mathematics*, *50*(2), 379–402. https://doi.org/10.1023/a:1003403601725

Ogata, Y., Katsura, K., Tsuruoka, H., & Hirata, N. (2019). High-resolution 3D earthquake forecasting beneath the greater Tokyo area. *Earth, Planets and Space*, *71*(1), 1–14. https://doi.org/10.1186/s40623-019-1086-7

Öncel, A. O., & Wyss, M. (2000). The major asperities of the 1999 Mw=7.4 Izmit earthquake defined by the microseismicity of the two decades before it. *Geophysical Journal International*, *143*(3), 501–506. https://doi.org/10.1046/j.1365-246x.2000.00211.x

Page, M. T., van der Elst, N., Hardebeck, J., Felzer, K., & Michael, A. J. (2016). Three ingredients for improved global aftershock forecasts: Tectonic region, time-dependent catalog incompleteness, and intersequence variability. *Bulletin of the Seismological Society of America*, *106*(5), 2290–2301. https://doi.org/10.1785/0120160073

Schoenberg, F. P. (2013). Facilitated estimation of ETAS. *Bulletin of the Seismological Society of America*, *103*(1), 601–605. https://doi.org/10.1785/0120120146

Scholz, C. (1968). The frequency-magnitude relation of microfracturing in rock and its relation to earthquakes. *Bulletin of the Seismological Society of America*, *58*(1), 399–415. https://doi.org/10.1785/bssa0580010399

Sharma, S., Hainzl, S., Zöeller, G., & Holschneider, M. (2020). Is Coulomb stress the best choice for aftershock forecasting? *Journal of Geophysical Research: Solid Earth*, *125*(9), e2020JB019553. https://doi.org/10.1029/2020jb019553

Spada, M., Tormann, T., Wiemer, S., & Enescu, B. (2013). Generic dependence of the frequency-size distribution of earthquakes on depth and its relation to the strength profile of the crust. *Geophysical Research Letters*, *40*(4), 709–714. https://doi.org/10.1002/grl.50093

Tahir, M., & Grasso, J. R. (2015). Faulting style controls for the space–time aftershock patterns. *Bulletin of the Seismological Society of America*, *105*(5), 2480–2497. https://doi.org/10.1785/0120140336

Tormann, T., Wiemer, S., & Hardebeck, J. L. (2012). Earthquake recurrence models fail when earthquakes fail to reset the stress field. *Geophysical Research Letters*, *39*(18), L18310. https://doi.org/10.1029/2012gl052913

Utsu, T. (1961). A statistical study on the occurrence of aftershocks. *Geophysical Magazine*, *30*, 521–605.

Wells, D. L., & Coppersmith, K. J. (1994). New empirical relationships among magnitude, rupture length, rupture width, rupture area, and surface displacement. *Bulletin of the Seismological Society of America*, *84*(4), 974–1002.

Werner, M. J., Helmstetter, A., Jackson, D. D., & Kagan, Y. Y. (2011). High-resolution long-term and short-term earthquake forecasts for California. *Bulletin of the Seismological Society of America*, *101*(4), 1630–1648. https://doi.org/10.1785/0120090340

Yang, W., & Ben-Zion, Y. (2009). Observational analysis of correlations between aftershock productivities and regional conditions in the context of a damage rheology model. *Geophysical Journal International*, *177*(2), 481–490. https://doi.org/10.1111/j.1365-246x.2009.04145.x

Zaliapin, I., & Ben-Zion, Y. (2013). Earthquake clusters in southern California II: Classification and relation to physical properties of the crust. *Journal of Geophysical Research: Solid Earth*, *118*(6), 2865–2877. https://doi.org/10.1002/jgrb.50178

Zaliapin, I., Gabrielov, A., Keilis-Borok, V., & Wong, H. (2008). Clustering analysis of seismicity and aftershock identification. *Physical Review Letters*, *101*(1), 018501. https://doi.org/10.1103/PhysRevLett.101.018501

Zhuang, J. (2011). Next-day earthquake forecasts for the Japan region generated by the etas model. *Earth, Planets and Space*, *63*(3), 207–216. https://doi.org/10.5047/eps.2010.12.010

Zhuang, J., Christophersen, A., Savage, M. K., Vere-Jones, D., Ogata, Y., & Jackson, D. D. (2008). Differences between spontaneous and triggered earthquakes: Their influences on foreshock probabilities. *Journal of Geophysical Research*, *113*(B11), B11302. https://doi.org/10.1029/2008jb005579

Zhuang, J., Ogata, Y., & Vere-Jones, D. (2002). Stochastic declustering of space-time earthquake occurrence. *Journal of the American Statistical Association*, *97*, 7369–7380.

Zhuang, J., Ogata, Y., & Vere-Jones, D. (2004). Analyzing earthquake clustering features by using stochastic reconstruction. *Journal of Geophysical Research*, *109*(B5), B05301. https://doi.org/10.1029/2003jb002879

References From the Supporting Information

Archuleta, R. J. (1984). A faulting model for the 1979 Imperial Valley earthquake. *Journal of Geophysical Research*, *89*(B6), 4559–4585. https://doi.org/10.1029/jb089ib06p04559

Bennett, R. A., Reilinger, R. E., Rodi, W., Li, Y., Toksöz, M. N., & Hudnut, K. (1995). Coseismic fault slip associated with the 1992 Mw 6.1 Joshua Tree, California, earthquake: Implications for the Joshua Tree-Landers earthquake sequence. *Journal of Geophysical Research*, *100*(B4), 6443–6461. https://doi.org/10.1029/94jb02944

Beroza, G. C. (1991). Near-source modeling of the Loma Prieta earthquake: Evidence for heterogeneous slip and implications for earthquake hazard. *Bulletin of the Seismological Society of America*, *81*(5), 1603–1621.

Beroza, G. C., & Spudich, P. (1988). Linearized inversion for fault rupture behavior: Application to the 1984 Morgan Hill, California, earthquake. *Journal of Geophysical Research*, *93*(B6), 6275–6296. https://doi.org/10.1029/jb093ib06p06275

Cohee, B. P., & Beroza, G. C. (1994). Slip distribution of the 1992 Landers earthquake and its implications for earthquake source mechanics. *Bulletin of the Seismological Society of America*, *84*(3), 692–712.

Cotton, F., & Campillo, M. (1995). Frequency domain inversion of strong motions: Application to the 1992 Landers earthquake. *Journal of Geophysical Research*, *100*(B3), 3961–3975. https://doi.org/10.1029/94jb02121

Custódio, S., Liu, P., & Archuleta, R. J. (2005). The 2004 Mw 6.0 Parkfield, California, earthquake: Inversion of near-source ground motion using multiple data sets. *Geophysical Research Letters*, *32*(23), L23312. https://doi.org/10.1029/2005gl024417

Dreger, D. (1994). Empirical green's function study of the January 17, 1994 Northridge, California earthquake. *Geophysical Research Letters*, *21*(24), 2633–2636. https://doi.org/10.1029/94gl02661

Dreger, D., Gee, L., Lombard, P., Murray, M. H., & Romanowicz, B. (2005). Rapid finite-source analysis and near-fault strong ground motions: Application to the 2003 Mw 6.5 San Simeon and 2004 Mw 6.0 Parkfield earthquakes. *Seismological Research Letters*, *76*(1), 40–48. https://doi.org/10.1785/gssrl.76.1.40

Emolo, A., & Zollo, A. (2005). Kinematic source parameters for the 1989 Loma Prieta earthquake from the nonlinear inversion of accelerograms. *Bulletin of the Seismological Society of America*, *95*(3), 981–994. https://doi.org/10.1785/0120030193

Hartzell, S. (1989). Comparison of seismic waveform inversion results for the rupture history of a finite fault: Application to the 1986 North Palm Springs, California, earthquake. *Journal of Geophysical Research*, *94*(B6), 7515–7534. https://doi.org/10.1029/jb094ib06p07515

Hartzell, S., & Heaton, T. H. (1983). Inversion of strong ground motion and teleseismic waveform data for the fault rupture history of the 1979 Imperial Valley, California, earthquake. *Bulletin of the Seismological Society of America*, *73*(6A), 1553–1583. https://doi.org/10.1785/bssa07306a1553

Hartzell, S., & Heaton, T. H. (1986). Rupture history of the 1984 Morgan Hill, California, earthquake from the inversion of strong motion records. *Bulletin of the Seismological Society of America*, *76*(3), 649–674. https://doi.org/10.1785/bssa0760030649

Hartzell, S., & Iida, M. (1990). Source complexity of the 1987 Whittier Narrows, California, earthquake from the inversion of strong motion records. *Journal of Geophysical Research*, *95*(B8), 12475–12485. https://doi.org/10.1029/jb095ib08p12475

Hartzell, S., Liu, P., & Mendoza, C. (1996). The 1994 Northridge, California, earthquake: Investigation of rupture velocity, risetime, and high-frequency radiation. *Journal of Geophysical Research*, *101*(B9), 20091–20108. https://doi.org/10.1029/96jb01883

Hernandez, B., Cotton, F., & Campillo, M. (1999). Contribution of radar interferometry to a two-step inversion of the kinematic process of the 1992 Landers earthquake. *Journal of Geophysical Research*, *104*(B6), 13083–13099. https://doi.org/10.1029/1999jb900078

Hough, S., & Dreger, D. (1995). Source parameters of the 23 April 1992 M 6.1 Joshua Tree, California, earthquake and its aftershocks: Empirical Green's function analysis of GEOS and TERRAscope data. *Bulletin of the Seismological Society of America*, *85*(6), 1576–1590.

Hudnut, K., Shen, Z., Murray, M., McClusky, S., King, R., Herring, T., et al. (1996). Co-seismic displacements of the 1994 Northridge, California, earthquake. *Bulletin of the Seismological Society of America*, *86*(1B), S19–S36. https://doi.org/10.1785/bssa08601b0s19

Jónsson, S., Zebker, H., Segall, P., & Amelung, F. (2002). Fault slip distribution of the 1999 Mw 7.1 Hector Mine, California, earthquake, estimated from satellite radar and GPS measurements. *Bulletin of the Seismological Society of America*, *92*(4), 1377–1389. https://doi.org/10.1785/0120000922

Kaverina, A., Dreger, D., & Price, E. (2002). The combined inversion of seismic and geodetic data for the source process of the 16 October 1999 Mw 7.1 Hector Mine, California, earthquake. *Bulletin of the Seismological Society of America*, *92*(4), 1266–1280. https://doi.org/10.1785/0120000907

Larsen, S., Reilinger, R., Neugebauer, H., & Strange, W. (1992). Global Positioning System measurements of deformations associated with the 1987 Superstition Hills earthquake: Evidence for conjugate faulting. *Journal of Geophysical Research*, *97*(B4), 4885–4902. https://doi.org/10.1029/92jb00128

Liu, H.-L., & Helmberger, D. V. (1983). The near-source ground motion of the 6 August 1979 Coyote Lake, California, earthquake. *Bulletin of the Seismological Society of America*, *73*(1), 201–218. https://doi.org/10.1785/bssa0730010201

Mendoza, C., & Hartzell, S. (1988). Inversion for slip distribution using teleseismic P waveforms: North Palm Springs, Borah Peak, and Michoacan earthquakes. *Bulletin of the Seismological Society of America*, *78*(3), 1092–1111. https://doi.org/10.1785/bssa0780031092

Mendoza, C., & Hartzell, S. (2013). Finite-fault source inversion using teleseismic P waves: Simple parameterization and rapid analysis. *Bulletin of the Seismological Society of America*, *103*(2A), 834–844. https://doi.org/10.1785/0120120069

Olson, A. H., & Apsel, R. J. (1982). Finite faults and inverse theory with applications to the 1979 Imperial Valley earthquake. *Bulletin of the Seismological Society of America*, *72*(6A), 1969–2001. https://doi.org/10.1785/bssa07206a1969

Steidl, J. H., Archuleta, R. J., & Hartzell, S. (1991). Rupture history of the 1989 Loma Prieta, California, earthquake. *Bulletin of the Seismological Society of America*, *81*(5), 1573–1602. https://doi.org/10.1785/bssa0810051573

Wald, D. J. (1992). Strong motion and broadband teleseismic analysis of the 1991 Sierra Madre, California, earthquake. *Journal of Geophysical Research*, *97*(B7), 11033–11046. https://doi.org/10.1029/92jb00565

Wald, D. J., & Heaton, T. H. (1994). Spatial and temporal distribution of slip for the 1992 Landers, California, earthquake. *Bulletin of the Seismological Society of America*, *84*(3), 668–691. https://doi.org/10.1785/bssa0840030668

Wald, D. J., Heaton, T. H., & Hudnut, K. W. (1996). The slip history of the 1994 Northridge, California, earthquake determined from strong-motion, teleseismic, GPS, and leveling data. *Bulletin of the Seismological Society of America*, *86*(1B), S49–S70. https://doi.org/10.1785/bssa08601b0s49

Wald, D. J., Helmberger, D. V., & Hartzell, S. (1990). Rupture process of the 1987 Superstition Hills earthquake from the inversion of strong-motion data. *Bulletin of the Seismological Society of America*, *80*(5), 1079–1098. https://doi.org/10.1785/bssa0800051079

Wald, D. J., Helmberger, D. V., & Heaton, T. H. (1991). Rupture model of the 1989 Loma Prieta earthquake from the inversion of strong-motion and broadband teleseismic data. *Bulletin of the Seismological Society of America*, *81*(5), 1540–1572. https://doi.org/10.1785/bssa0810051540

Wei, S., Helmberger, D., Owen, S., Graves, R. W., Hudnut, K. W., & Fielding, E. J. (2013). Complementary slip distributions of the largest earthquakes in the 2012 Brawley swarm, Imperial Valley, California. *Geophysical Research Letters*, *40*(5), 847–852. https://doi.org/10.1002/grl.50259

Zeng, Y., & Anderson, J. (2000). Evaluation of numerical procedures for simulating near-fault long-period ground motions using Zeng method. Report 2000/01 to the PEER Utilities Program. Retrieved from http://peer.berkeley.edu